

Article

# Selective NO<sub>2</sub> Detection by Black Phosphorus Gas Sensor Prepared via Aqueous Route for Ship Pollutant Monitoring

Yang Wang, Yujia Wang, Yue Sun, Kuanguang Zhang, Chenyang Zhang, Jianqiao Liu \*, Ce Fu \*  
and Junsheng Wang \*

College of Information Science and Technology, Dalian Maritime University, Dalian 116026, China

\* Correspondence: jqliu@dmlu.edu.cn (J.L.); fuce\_dmlu@sina.com (C.F.); wangjsh@dmlu.edu.cn (J.W.);

Tel.: +86-411-84729934 (J.L.)

**Abstract:** The emission of nitrogen dioxide (NO<sub>2</sub>) caused by marine transportation has attracted worldwide environmental concerns. Two-dimensional (2D) black phosphorus (BP) is an emerging semiconductive material with the advantages of high electron mobility, a layer-dependent direct band gap and a large specific surface area. These properties ensure excellent potential in gas-sensing applications. In this work, BP quantum dots (QDs) are synthesized from commercial red phosphorus (RP) fine powder via the aqueous route. The BP QDs show uniform size distribution with an average size of 2.2 nm. They are employed to fabricate thin film gas sensors by aerial-assisted chemical vapor deposition. The microstructure, morphology and chemical composition are determined by various characterizations. The sensor performances are evaluated with the optimized response set to 100 ppm NO<sub>2</sub> of 10.19 and a sensitivity of 0.48 is obtained. The gas sensor also demonstrates excellent repeatability, selectivity and stability. The fabricated thin film gas sensor assembled by BP QDs exhibits prospective applications in selective NO<sub>2</sub> detection for marine gaseous pollutant monitoring and control.



**Citation:** Wang, Y.; Wang, Y.; Sun, Y.; Zhang, K.; Zhang, C.; Liu, J.; Fu, C.; Wang, J. Selective NO<sub>2</sub> Detection by Black Phosphorus Gas Sensor Prepared via Aqueous Route for Ship Pollutant Monitoring. *J. Mar. Sci. Eng.* **2022**, *10*, 1892. <https://doi.org/10.3390/jmse10121892>

Academic Editor: Christos Tsabaris

Received: 29 October 2022

Accepted: 23 November 2022

Published: 4 December 2022

**Publisher's Note:** MDPI stays neutral with regard to jurisdictional claims in published maps and institutional affiliations.



**Copyright:** © 2022 by the authors. Licensee MDPI, Basel, Switzerland. This article is an open access article distributed under the terms and conditions of the Creative Commons Attribution (CC BY) license (<https://creativecommons.org/licenses/by/4.0/>).

**Keywords:** black phosphorus quantum dot; 2D material; NO<sub>2</sub> detection; ship pollutant monitoring; semiconductor gas sensor

## 1. Introduction

The rapid development of marine transportation driven by growing global trade and economic activities leads to a huge amount of gaseous pollutant emissions into the atmosphere [1]. Among them, nitrogen dioxide (NO<sub>2</sub>) is considered a priority impactive pollutant as it may lead to acid rain, eutrophication, acidity of surface water and, consequently, toxicity to living creatures [2–9]. Therefore, the monitoring of ship exhausts, especially nitrogen dioxide emission, has attracted worldwide environmental concerns.

Two-dimensional (2D) nanostructures are emerging candidates for developing semiconductor gas sensors with superior properties [10–13]. Compared to traditional gas sensors involving semiconductor bulks, the 2D nanostructures have the advantage of a large specific surface area, abundant active dangling bonds, and high carrier mobility [14]. Among 2D materials, such as transition metal dichalcogenides [15], graphic-like carbon nitrides (g-C<sub>3</sub>N<sub>4</sub>) [16], reduced-graphene oxide (rGO) [17], hexagonal-boron nitride (h-BN) [18], and transition metal carbide [19], black phosphorus (BP) is attractive due to the controllable direct band gap, free of metal elements and biocompatibility [20–25]. These unique properties provide great potential and suitability in applications of high-performance electronic components [26,27], photocatalysis [28,29] and medical treatments [30,31].

The BP-based nanostructures were soon put into the development of gas sensors. M. Donarelli's early work prepared exfoliated BP flakes for an NO<sub>2</sub> gas sensor, but the performance was quite low [32]. G. Lee used suspended BP flakes and the device showed a response of 2.86 to 200 ppm target gas [33]. To improve the performance of BP-based

gas sensors, Ag-decorated BP nanosheets were prepared by Y. Wang [34] and an Au incorporation into the BP matrix was completed by S. Cho [35]. Thus, the limit of detection (LOD) was significantly lowered to sub-ppm level. The combination of BP nanostructures with other semiconductors was also developed to construct heterojunctions for improved sensor performances [36–39].

However, the synthesis of BP nanostructures and the fabrication of their subsequent electronic devices were rather complex. Mechanical exfoliation was the most popular method in the early stages. The BP bulk, which was stacked by phosphorene connected by Van der Waals force, was exfoliated mechanically, e.g., by tapes. The obtained few-layer BP structures were cleaned using organic solvents and sent for the fabrication of gas sensors on substrates. For instance, by using these procedures, Cui prepared a field-effect transistor sensor device based on BP nanosheets, which showed a response of 1.9 to 20 ppb NO<sub>2</sub> with good repeatability [40]. Similarly, Lee's work reported the platinum functionalization of BP gas sensors, which exhibited a response of 1.6 to 4000 ppm H<sub>2</sub> at 100 °C [41]. Nevertheless, the mechanical exfoliation required by specific facilities were unable to be operated under ambient conditions, restricting the yield of BP nanostructures. Another technique that developed later was liquid exfoliation, which used ultrasonic facilities to destroy the layered structure of bulk BP. This method was successful in providing a high yield of BP nanostructures but it required the extensive usage of organic solvents, where the BP bulk was disassembled. Chen exfoliated BP bulk into highly-dispersed BP nanosheets in N-methylpyrrolidone and fabricated BP-based gas sensors, but the response was unsatisfactory [42]. Wang synthesized BP nanosheets from bulk in diethylene glycol dimethyl ether by ultrasonication in ice water and the obtained nanostructures were used to prepare BP-based gas sensors, which demonstrated a fast response and recovery [43]. However, the liquid exfoliation was facing fatal drawbacks of non-uniform size and morphology as well as an uncontrollable nanostructure. Despite the excellent properties and great potential of BP-based gas sensors, their practical application was restricted by complicated and expensive synthesis procedures. A simple synthesis technique for BP nanostructures with environmental and cost considerations is expected.

In this work, a facile aqueous synthesis of BP quantum dots (BP QDs) from commercial red phosphorus (RP) is developed without using toxic and explosive organic solvents. The BP QDs are used to fabricate thin film gas sensors for NO<sub>2</sub> detection by aerial-assisted chemical vapor deposition (AACVD). The BP QDs and their subsequent thin films are characterized in the aspects of microstructure, morphology and elemental compositions. The optimized deposition conditions of thin films are concluded and the gas-sensing performances of response, sensitivity, repeatability, selectivity and stability are evaluated. The gas-sensing mechanism of BP thin films in NO<sub>2</sub> detection is also interpreted.

## 2. Materials and Methods

### 2.1. Aqueous Preparation of BP

All chemicals used in this work are analytical reagents obtained from Sinopharm Chemical Reagent Co., Ltd. (Shanghai, China). The BP QDs were synthesized via a one-step aqueous route [44], which is illustrated in Figure 1.

The initial RP was cracked and passed through a mesh to obtain an RP fine powder with a particle size less than 106 μm. The RP fine powder of 0.2 g was dispersed by 16.2 mL deionized water (DI) in a polyphenylene autoclave, which was sent for hydrothermal treatment, conducted at 200 °C for 48 h before cooling to room temperature. After this process, the RP fine powder was transformed into BP QDs in the aqueous solution.

### 2.2. Deposition of BP Gas Sensors

The BP gas sensors were fabricated by using the AACVD method [45], which is illustrated in Figure 2. The alumina substrates, on which a pair of Ag interdigital electrodes were designed, were cleaned and placed in the tube. The BP QD aqueous solution was atomized and delivered by the N<sub>2</sub> carrier gas with a flux of 100 sccm into the tube. The

deposition was conducted at 250–450 °C and, thus, the BP thin films were obtained after the QDs were deposited on the alumina substrates.

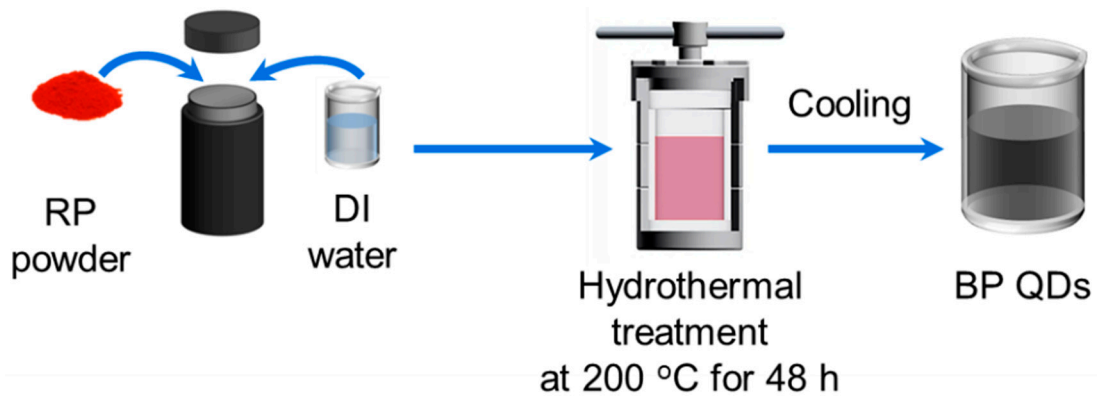


**Figure 1.** Aqueous preparation procedure of BP QDs from RP via the hydrothermal method.

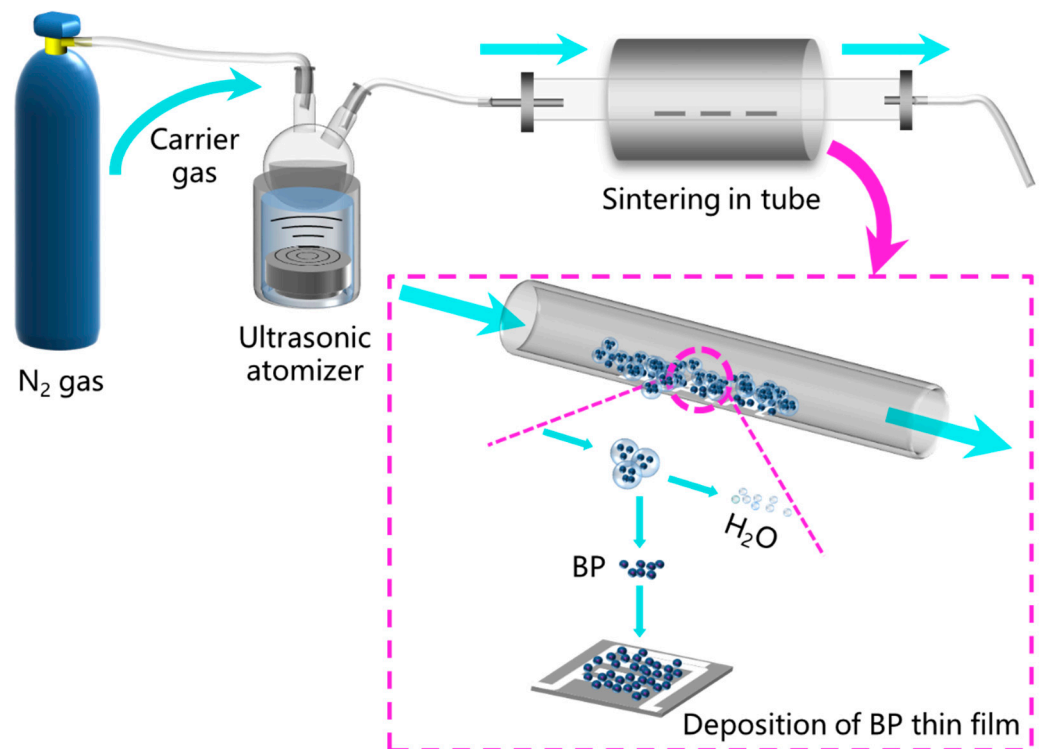


**Figure 2.** AACVD procedure of BP thin film gas sensors.

### 2.3. Characterization

A high-resolution transmission electron microscopy (HRTEM, JEM-2100F, JEOL, Tokyo, Japan) and X-ray diffraction (XRD, D/Max-Ultima, Rigaku, Tokyo, Japan) were used to observe the microstructural properties of the BP QDs. The surface chemical characteristics were collected via X-ray photoelectron spectroscopy (XPS, ESCALAB 250XI, Thermo Fisher Scientific, Waltham, MA, USA). The surface morphology and compositional mappings of the BP thin film sensors were evaluated via scanning electron microscopy (SEM, ZEISS Gemini 500, Carl Zeiss AG, Oberkochen, Germany) with the component of energy dispersive spectroscopy (EDS). The BP QD aqueous solution was used in the HRTEM characterization. The BP containing solution was sprayed onto quartz pieces and dried in an oxygen free atmosphere before XPS and EDS analyses. The BP thin film gas sensors were sent to SEM observation after the AACVD procedures.

#### 2.4. Measurement of Gas-Sensing Properties

All evaluations of the sensor performance of the BP thin film were conducted at room temperature (25 °C) and a relative humidity (RH) of 40%, except for the humidity dependence evaluation. High purity (>99%) gases of C<sub>4</sub>H<sub>10</sub>, H<sub>2</sub>, H<sub>2</sub>S and NO<sub>2</sub> were used as target gases. A computer-controlled gas-sensing measurement system [46,47] was used to collect the resistance of the BP thin films. The response (S) was defined as the resistance change of the sensor after gas exposure, calculated by  $S = R_a/R_g$ , where  $R_a$  and  $R_g$  were the resistance in the air and in the target gas, respectively. The response time ( $T_{res}$ ) and recovery time ( $T_{rec}$ ) were defined as the times needed for the gas sensor to reach 90% resistance variation after injection or removal of the target gas. The sensitivity indicated the sensor response led by the unit change in gas concentration. Mathematically, it was calculated by the slope ( $n$ ) of the response against the gas concentration in the logarithmic coordinates, as  $n = \ln S / \ln C$ .

### 3. Results and Discussion

#### 3.1. Characterization of BP QDs

The microstructural properties and morphology of the as-synthesized BP QDs is shown in Figure 3. The HRTEM observation in Figure 3a shows that the BP QDs are of good dispersion in aqueous solution. Figure 3b demonstrates the size distribution of BP QDs, which indicates that the average size is approximately 2.8 nm. The high-resolution lattice fringes are clearly exhibited in Figure 3c. The fringe spacing of 0.21 nm is revealed and is associated with the (021) facet of the BP crystal lattice [48]. The XRD pattern of BP QDs is revealed in Figure 3d. The sole peak at 27.3° is observed, corresponding to the (021) facet of the BP lattice structure as listed in the standard pattern of JCPDS 01-076-1967 [49]. The broad shape of the peak infers the tiny crystallite structure of the BP QDs. Based on the Debye–Scherrer equation, the crystallite size is evaluated to be 2.5 nm, close to the HRTEM observation.

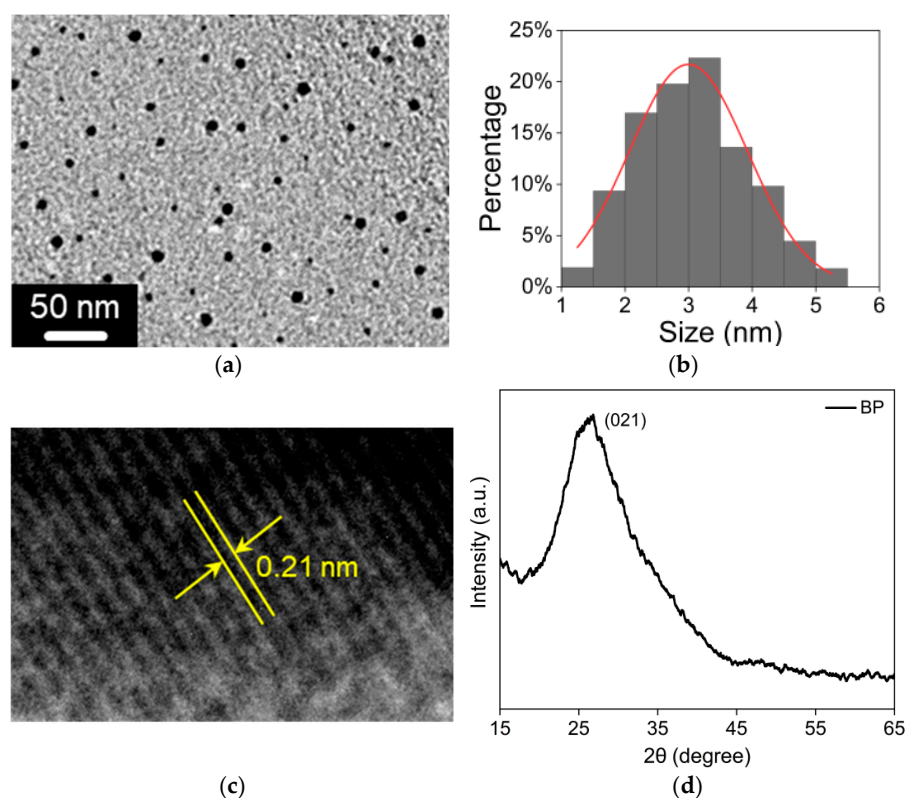


**Figure 3.** Microstructural properties of BP QDs in aqueous solution: (a) Morphology; (b) High-resolution lattice fringes; (c) Size distribution; (d) XRD pattern.

Figure 4a demonstrates the XPS survey spectrum of the BP thin films. All of the peaks are calibrated using the C peak at 284.8 eV [50,51]. The survey spectrum demonstrates the presence of P, O, Si, N and C. The tiny nitrous signal is ascribed to the impurities led by the N<sub>2</sub> carrier gas during the deposition process, while the Si peak is caused by the quartz substrates used in the XPS characterizations. The high-resolution spectrum for the P element is revealed in Figure 4b, where double peaks at 130.48 eV and 134.78 eV are observed. The former one is assigned to the P 2p peak [52] while the latter one is ascribed to the phosphorus oxide (PO<sub>x</sub>) [53]. Thus, the as-synthesized BP QDs in aqueous solution are partially-oxidized. The O spectrum is exhibited in Figure 4c and is composed of double peaks at 531.78 eV and 532.18 eV. The high intensity peak is ascribed to the O-P-O bonds and the other one is caused by the bivalent bond (P=O) in oxidized phosphorus. Apart from the surface bonding properties evaluated by the XPS, the bulk composition of the BP QDs is analyzed by EDS, as shown in Figure 4d. The main signals of phosphorus and oxygen are detected together with silicon in the quartz substrates. The peak area proportion of each element is employed to evaluate the elemental composition of the sample. After deducting the stoichiometric O atoms of SiO<sub>2</sub> in the quartz substrate, the P/O ratio is calculated to be 1.6, inferring that 1/4 of the P atoms in the BP structure are in the oxidizing state.

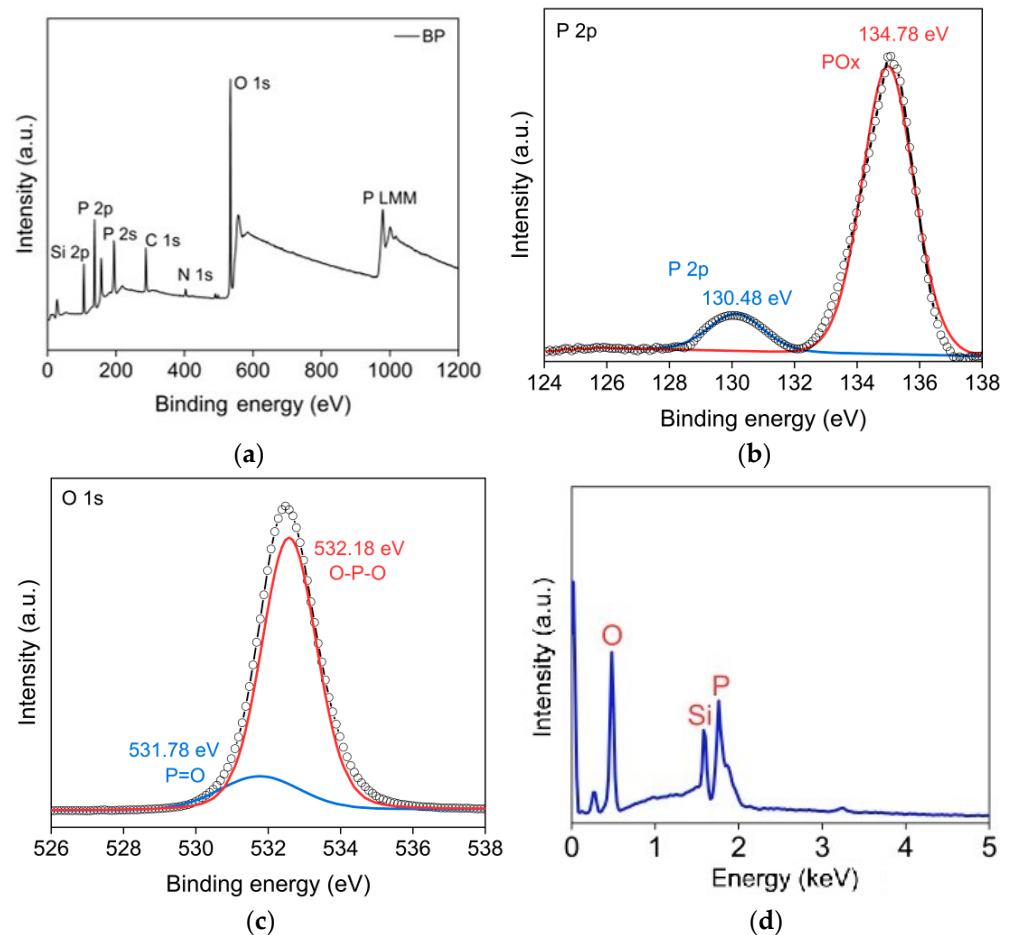


**Figure 4.** Compositional properties of BP QDs: (a) XPS survey spectrum; (b) XPS P 2p spectrum; (c) XPS O 1s spectrum; (d) EDS spectrum.

### 3.2. Characterizations of BP Gas Sensors

The surface morphology of the gas sensor deposited by the BP QDs is revealed in Figure 5a,b, where BP grains of 100–500 nm are uniformly scattered on the substrate. The average grain size is evaluated to be 310 nm. The scattered distribution of the BP grains provides a large specific surface area with rich active sites for gas absorption, which is constructive for the enhancement of the gas-sensing properties. Figure 5c–e demonstrate the

surface composition of the BP thin film sensors. P and O are detected and they show spatial uniformity. The existence of O comes from the partial oxidation of the as-prepared BP QDs. The partial oxidation of the thin film surface may protect the inner part and prevent further oxidation during gas detection in ambient condition [54,55]. This is beneficial for permanent stability of BP thin films.

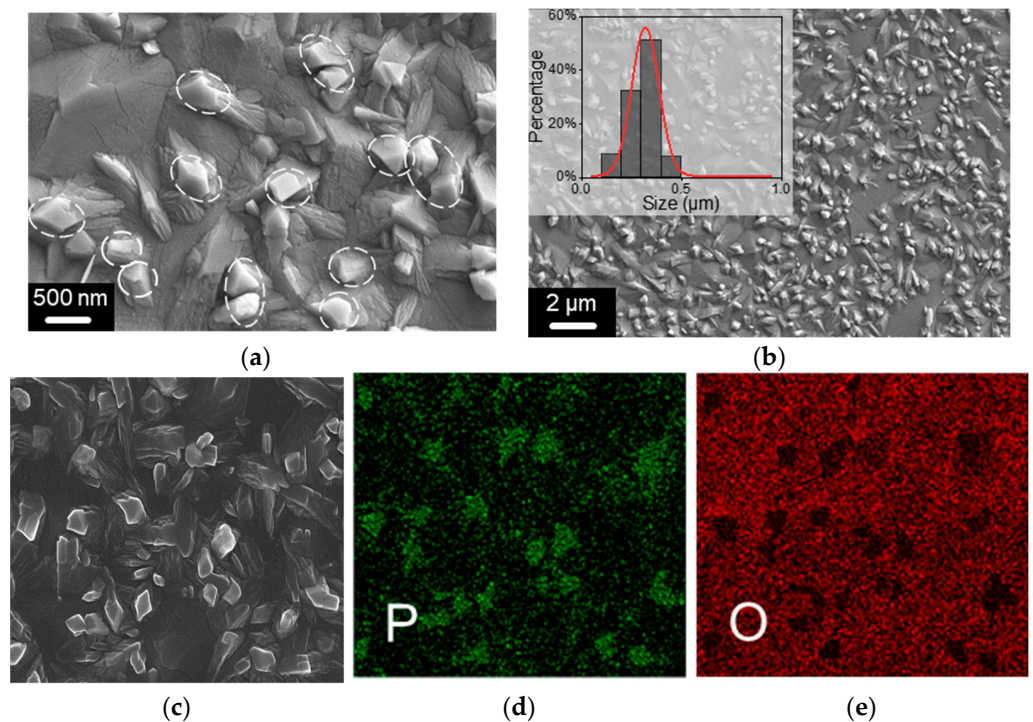


**Figure 5.** Microstructural and compositional properties of the BP thin film sensor: (a) SEM morphology; (b) SEM morphology with size distribution of grains; (c) Local morphology for elemental mapping; (d) Elemental distribution of P atoms; (e) Elemental distribution of O atoms.

### 3.3. Gas-sensing Properties

The gas sensors are tested under the exposure of 100 ppm  $\text{NO}_2$ . Figure 6a exhibits the kinetic response of the BP thin films deposited for 30 min at the temperatures of 250, 300, 350, 400 and 450 °C. The  $T_{\text{res}}$  and  $T_{\text{rec}}$  are 36 s/162 s, 51 s/565 s, 38/844 s, 91 s/174 s and 48 s/108 s, respectively. The sensor responses are 1.56, 2.49, 10.19, 1.41 and 1.07, respectively, as shown in Figure 6c together with their initial resistances in air. It is observed that the BP thin film deposited at 350 °C has an optimized response and response time. The dependence of gas-sensing properties on deposition time is also illustrated in Figure 6b, in which the BP thin film is deposited at 350 °C. The deposition times of 15–75 min were conducted and the  $T_{\text{res}}/T_{\text{rec}}$  of the thin films were 123 s/223 s, 38 s/844 s, 40 s/103 s, 89 s/95 s and 100 s/516 s, respectively. The sensor responses of 1.22, 10.19, 4.18, 1.64 and 1.40 are observed, respectively, as shown in Figure 6d, together with their initial resistances in air. The optimum gas-sensing performances were obtained for the BP thin film deposited at 350 °C for 30 min. This optimized deposition condition was used in the successive preparation of the BP gas sensors.

Figure 7a shows the dynamic response of the BP gas sensor deposited at 350 °C for 30 min to various concentrations of  $\text{NO}_2$  gas. The resistance of the BP thin film responds to the exposure to target gas of 20–100 ppm and has a complete recover ability. The sensor responses are calculated and plotted in both of the linear and logarithmic coordinates, as shown in Figure 7b. The response against the gas concentration follows the power law [56,57], which describes the saturation effect of sensors in a high concentration of target gas. Based on the logarithmic relation, the sensitivity is evaluated to be 0.48, which infers that the thin film gas sensor deposited by the BP QDs has excellent

gas-sensing performance. The theoretical LOD of the BP gas sensor is evaluated to be 0.54 ppm, based on the root-mean square deviation (RMSD) and sensitivity, according to  $LOD = 3 \times RMSD/sensitivity$  [34].

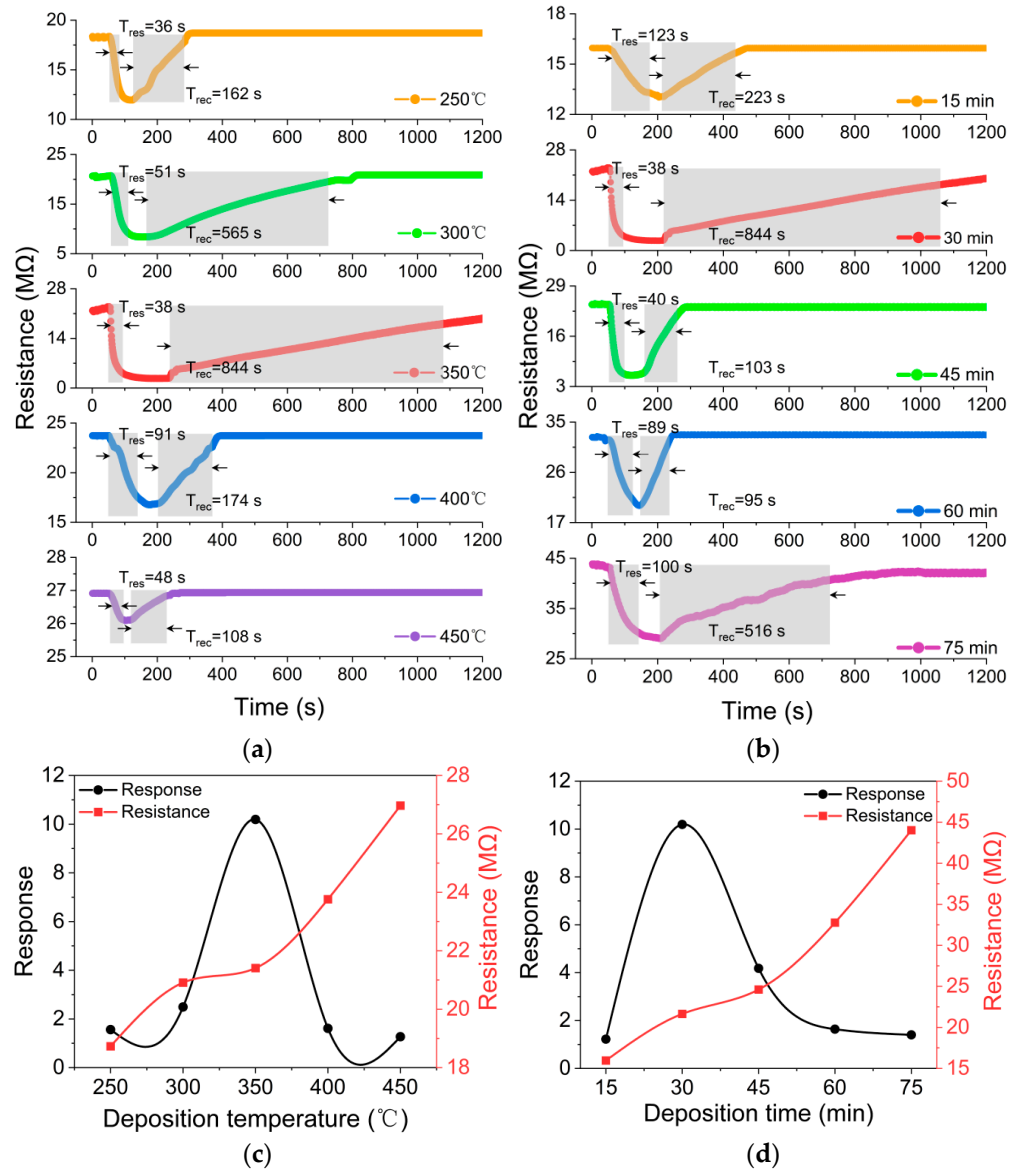


**Figure 6.** Gas-sensing properties of BP thin films: (a) Thin films deposited under various temperatures; (b) Thin films deposited under various times; (c) Influence of deposition temperature; (d) Influence of deposition time.

Repeatability and selectivity are the other two fundamental properties for gas sensors. Figure 8a demonstrates the repeatability test of the BP gas sensor, which exhibits a consistent response to 100 ppm NO<sub>2</sub> among four cycles of 800 s. The selectivity test is conducted by using the target gases NO<sub>2</sub>, H<sub>2</sub>S, H<sub>2</sub> and C<sub>4</sub>H<sub>10</sub>. The response to the four types of gases at 20 and 100 ppm are shown in Figure 8b. As the p-type nature of BP thin film, the sensor shows a response below 1 when reducing H<sub>2</sub>S gas is tested. Meanwhile, the BP thin film is insensitive to H<sub>2</sub> and C<sub>4</sub>H<sub>10</sub>. The dependence of sensor performance on humidity is shown in Figure 8c, where a slight decrease in response is observed, showing that the BP thin film shows good stability against humidity. The insensitive RH dependence could be ascribed to the partially-oxidized surface of the BP thin film. Nevertheless, humidity corrections or compensations could be carried out if precise detection is required. The sensor resistance in this work is in the range of 10–50 MΩ, which is at the same level with

sensors from previous works [58]. The time-dependent resistance of thin film is evaluated within 30 days. As shown in Figure 8d, the sensor resistance demonstrates general stability over time. A minor increase in resistance is observed after 10 days and this could be due to further slight oxidation of the BP thin films. Therefore, the as-prepared BP thin film gas sensor demonstrates excellent repeatability, selectivity and stability in the detection of NO<sub>2</sub> gas. The NO<sub>2</sub> sensing performance of the BP-based gas sensor is compared in Table 1. The present BP thin film gas sensor has superior gas-sensing properties to other published devices.

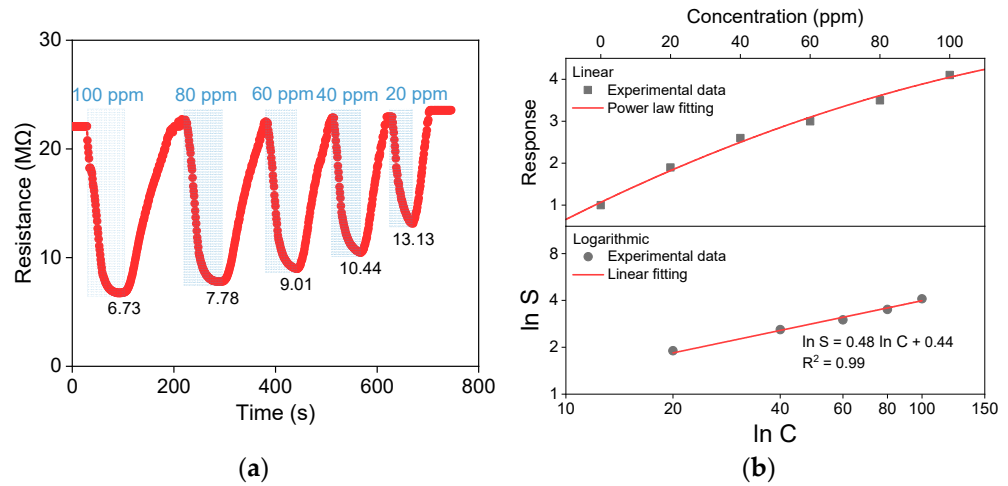


**Figure 7.** Gas-sensing properties of BP gas sensors deposited at 350 °C for 30 min: (a) Dynamic sensor response to various gas concentrations; (b) Evaluation of sensor sensitivity.

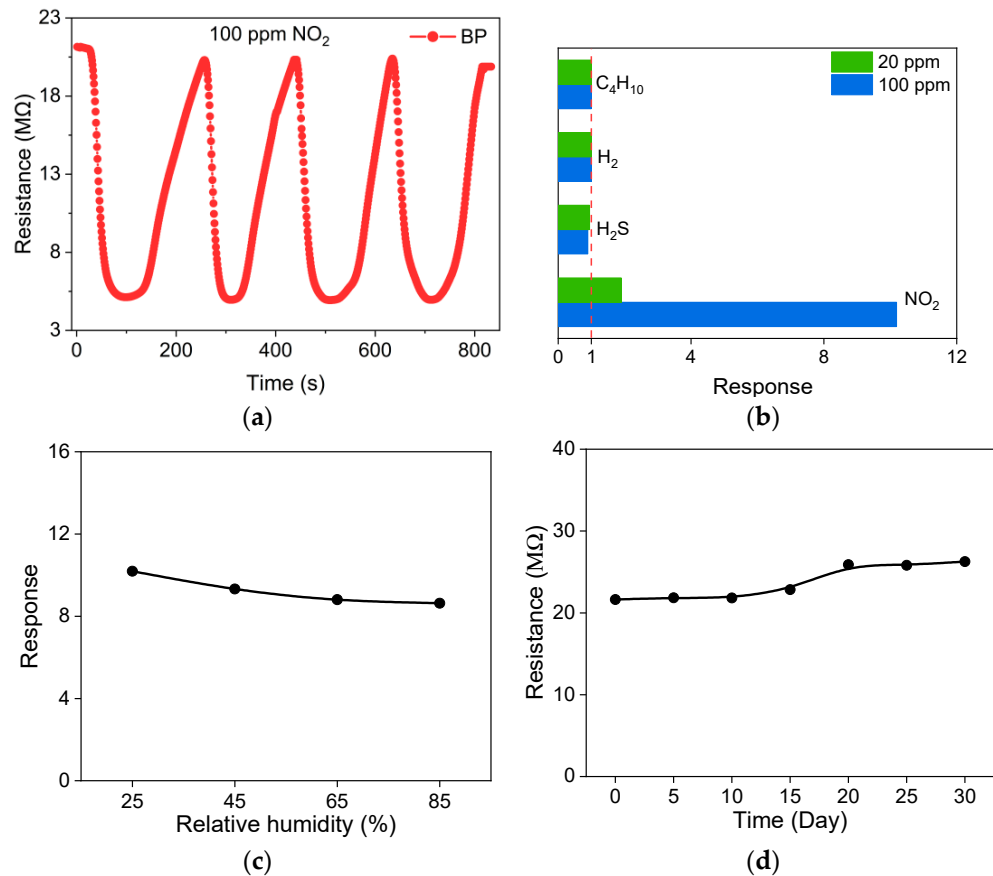


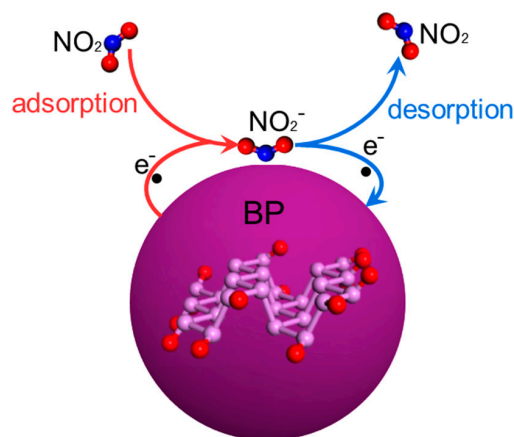
**Figure 8.** The repeatability, selectivity and stability evaluation of BP thin films deposited at 350 °C for 30 min: (a) Repeatability test; (b) Selectivity test; (c) RH dependence; (d) Resistance stability over time.

**Table 1.** Comparison of NO<sub>2</sub> sensing performances of the BP-based gas sensors.

Reference	Composition	Concentration (ppm)	Operating Temperature (°C)	Response
[32]	BP flakes	0.2	25	1.08
[33]	BP flakes	200	N/A	2.86
[34]	Ag-decorated BP	0.1	22	1.67
[35]	Au-incorporated BP	1	25	3.33
[36]	Co <sub>3</sub> O <sub>4</sub> -PEI-BP	3	25	2.86
[37]	ZnO-BP	0.05	25	3.85
[38]	SnS <sub>2</sub> -BP	0.1	25	6.08
[39]	MXene-BP	10	20	1.24
This work	BP thin film	100	25	10.19

### 3.4. Gas-Sensing Mechanism

The development of BP gas sensors will benefit if the process of gas detection is well understood. Figure 9 demonstrates the gas-sensing mechanism of BP gas sensors. When the BP is exposed to NO<sub>2</sub>, the oxidizing gas species will adsorb on the surface of the BP grains. The adsorbates of NO<sub>2</sub><sup>-</sup> capture electrons from the P atoms on the grain surface, resulting in the decrease of electron density as well as the increase in hole density. As the p-type characteristics of BP, the sensor resistance is decreased, exhibiting an electrical response to NO<sub>2</sub> gas. On the other hand, when NO<sub>2</sub> gas is removed from the atmosphere, the BP thin film desorbs the NO<sub>2</sub><sup>-</sup> species and the electrons that were seized by the adsorbates are returned to the semiconductor. Thus, the resistance of the BP thin film recovers to the initial value.

**Figure 9.** Schematic drawing of the gas-sensing mechanism of the BP sensor to NO<sub>2</sub>.

## 4. Conclusions

BP QDs were synthesized in an aqueous solution via a one-step hydrothermal method. They were employed to fabricate BP thin film using the AACVD technique. The microstructural, morphological and compositional properties of the BP QDs and thin films were evaluated by HRTEM, XRD, XPS, SEM and EDS characterizations. Several conclusions were drawn as follows:

- The BP QDs were prepared from RP fine powder under low temperature, without using any toxic or explosive organic solvents.
- The BP thin films deposited from QDs exhibited good gas-sensing performance and optimized sensor properties were obtained from the BP gas sensors deposited at 350 °C for 30 min.
- The optimum response to 100 ppm NO<sub>2</sub> was 10.19 with a sensor sensitivity of 0.48. The BP thin film gas sensor also demonstrated excellent recovery ability, repeatability, selectivity and stability. The present BP thin film gas sensor has superior gas-sensing properties to other published devices.

This work not only accomplished the design of a BP thin film gas sensor with promising prospects for the selective detection of gaseous ship pollutants, but also contributes to a green strategy for the fabrication of 2D BP-based semiconductor devices.

**Author Contributions:** Conceptualization, Y.W. (Yang Wang) and J.L.; methodology, Y.W. (Yujia Wang), Y.S., K.Z. and C.Z.; investigation, Y.S., K.Z. and C.Z.; writing—original draft preparation, Y.W. (Yang Wang) and J.L.; writing—review and editing, C.F. and J.W.; project administration, C.F. and J.W.; funding acquisition, J.L. All authors have read and agreed to the published version of the manuscript.

**Funding:** This work is financially supported by the International Science & Technology Innovation Program of the Chinese Academy of Agricultural Sciences (Grant No. CAAS-ZDRW202110), the Scientific Research Funding Project of the Educational Department of Liaoning Province (Grant No. LJKZ0060), the Liaoning Applied Fundamental Research Project (Grant No. 2022JH2/101300158) and the Fundamental Research Funds for the Central Universities (Grant No. 3132022238).

**Institutional Review Board Statement:** Not applicable.

**Informed Consent Statement:** Not applicable.

**Data Availability Statement:** The data presented in this study are available on request from the corresponding author.

**Acknowledgments:** We appreciate Eceshi ([www.eceshi.com](http://www.eceshi.com) (accessed on 25 October 2022)) for the XRD and XPS characterizations.

**Conflicts of Interest:** The authors declare no conflict of interest.

## References

1. Aminzadegan, S.; Shahriari, M.; Mehranfar, F.; Abramović, B. Factors affecting the emission of pollutants in different types of transportation: A literature review. *Energy Rep.* **2022**, *8*, 2508–2529. [[CrossRef](#)]
2. Wang, R.; Bei, N.; Wu, J.; Li, X.; Liu, S.; Yu, J.; Jiang, Q.; Tie, X.; Li, G. Cropland nitrogen dioxide emissions and effects on the ozone pollution in the North China plain. *Environ. Pollut.* **2022**, *294*, 118617. [[CrossRef](#)] [[PubMed](#)]
3. de Vries, W. Impacts of nitrogen emissions on ecosystems and human health: A mini review. *Curr. Opin. Environ. Sci. Health* **2021**, *21*, 100249. [[CrossRef](#)]
4. Chen, J. Mitigating nitrogen dioxide air pollution: The roles and effect of national smart city pilots in China. *Energy* **2023**, *263*, 125652. [[CrossRef](#)]
5. Costa, S.; Ferreira, J.; Silveira, C.; Costa, C.; Lopes, D.; Relvas, H.; Borrego, C.; Roebeling, P.; Miranda, A.I.; Paulo Teixeira, J. Integrating health on air quality assessment—Review report on health risks of two major european outdoor air pollutants: PM and NO<sub>2</sub>. *J. Toxicol. Environ. Health Part B* **2014**, *17*, 307–340. [[CrossRef](#)]
6. Tao, Y.; Mi, S.; Zhou, S.; Wang, S.; Xie, X. Air pollution and hospital admissions for respiratory diseases in Lanzhou, China. *Environ. Pollut.* **2014**, *185*, 196–201. [[CrossRef](#)]
7. Zeng, W.; Zhao, H.; Liu, R.; Yan, W.; Qiu, Y.; Yang, F.; Shu, C.; Zhan, Y. Association between NO<sub>2</sub> cumulative exposure and influenza prevalence in mountainous regions: A case study from southwest China. *Environ. Res.* **2020**, *189*, 109926. [[CrossRef](#)] [[PubMed](#)]
8. Naidoo, R.N. NO<sub>2</sub> increases the risk for childhood asthma: A global concern. *Lancet Planet. Health* **2019**, *3*, e155–e156. [[CrossRef](#)]
9. Achakulwisut, P.; Brauer, M.; Hystad, P.; Anenberg, S.C. Global, national, and urban burdens of paediatric asthma incidence attributable to ambient NO<sub>2</sub> pollution: Estimates from global datasets. *Lancet Planet. Health* **2019**, *3*, e166–e178. [[CrossRef](#)]
10. Jiang, H.-L.; Pan, J.; Zhou, W.; Li, H.-M.; Liu, S. Fabrication and application of arrays related to two-dimensional materials. *Rare Met.* **2022**, *41*, 262–286. [[CrossRef](#)]
11. Zhang, H.-F.; Xuan, J.-Y.; Zhang, Q.; Sun, M.-L.; Jia, F.-C.; Wang, X.-M.; Yin, G.-C.; Lu, S.-Y. Strategies and challenges for enhancing performance of MXene-based gas sensors: A review. *Rare Met.* **2022**, *41*, 3976–3999. [[CrossRef](#)]
12. Zhao, Q.-N.; Zhang, Y.-J.; Duan, Z.-H.; Wang, S.; Liu, C.; Jiang, Y.-D.; Tai, H.-L. A review on Ti<sub>3</sub>C<sub>2</sub>T<sub>x</sub>-based nanomaterials: Synthesis and applications in gas and humidity sensors. *Rare Met.* **2021**, *40*, 1459–1476. [[CrossRef](#)]
13. Galstyan, V.; Moumen, A.; Kumarage, G.W.C.; Comini, E. Progress towards chemical gas sensors: Nanowires and 2D semiconductors. *Sens. Actuators B* **2022**, *357*, 131466. [[CrossRef](#)]
14. Erande, M.B.; Pawar, M.S.; Late, D.J. Humidity sensing and photodetection behavior of electrochemically exfoliated atomically thin-layered black phosphorus nanosheets. *ACS Appl. Mat. Interfaces* **2016**, *8*, 11548–11556. [[CrossRef](#)] [[PubMed](#)]
15. Zheng, W.; Liu, X.; Xie, J.; Lu, G.; Zhang, J. Emerging van der Waals junctions based on TMDs materials for advanced gas sensors. *Coord. Chem. Rev.* **2021**, *447*, 214151. [[CrossRef](#)]

16. Ghosh, R.; Aslam, M.; Kalita, H. Graphene derivatives for chemiresistive gas sensors: A review. *Mater. Today Commun.* **2022**, *30*, 103182. [[CrossRef](#)]
17. Ding, J.; Dai, H.; Chen, H.; Jin, Y.; Fu, H.; Xiao, B. Highly sensitive ethylene glycol gas sensor based on ZnO/rGO nanosheets. *Sens. Actuators B* **2022**, *372*, 132655. [[CrossRef](#)]
18. Jibril Ibrahim, A.; Ghani, H.A.; Hussein, E.S.; Abdullaha, S.A.H.; Kadhim, M.M.; Mahdi Rheima, A.; Turki Jalil, A.; Anshul, Y. Metal-decorated BN monolayer as potential chemical sensors for detection of purinethol drug. *Inorg. Chem. Commun.* **2022**, *145*, 109919. [[CrossRef](#)]
19. Huang, W.-X.; Li, Z.-P.; Li, D.-D.; Hu, Z.-H.; Wu, C.; Lv, K.-L.; Li, Q. Ti<sub>3</sub>C<sub>2</sub> MXene: Recent progress in its fundamentals, synthesis, and applications. *Rare Met.* **2022**, *41*, 3268–3300. [[CrossRef](#)]
20. Guo, Z.; Ding, W.; Liu, X.; Sun, Z.; Wei, L. Two-dimensional black phosphorus: A new star in energy applications and the barrier to stability. *Appl. Mater. Today* **2019**, *14*, 51–58. [[CrossRef](#)]
21. Xing, C.; Zhang, J.; Jing, J.; Li, J.; Shi, F. Preparations, properties and applications of low-dimensional black phosphorus. *Chem. Eng. J.* **2019**, *370*, 120–135. [[CrossRef](#)]
22. Qin, L.; Jiang, S.; He, H.; Ling, G.; Zhang, P. Functional black phosphorus nanosheets for cancer therapy. *J. Control. Release* **2020**, *318*, 50–66. [[CrossRef](#)] [[PubMed](#)]
23. Wu, Y.; Yuan, W.; Xu, M.; Bai, S.; Chen, Y.; Tang, Z.; Wang, C.; Yang, Y.; Zhang, X.; Yuan, Y.; et al. Two-dimensional black phosphorus: Properties, fabrication and application for flexible supercapacitors. *Chem. Eng. J.* **2021**, *412*, 128744. [[CrossRef](#)]
24. Zhang, Y.; Jiang, Q.; Lang, P.; Yuan, N.; Tang, J. Fabrication and applications of 2D black phosphorus in catalyst, sensing and electrochemical energy storage. *J. Alloys Compd.* **2021**, *850*, 156580. [[CrossRef](#)]
25. Zhong, Q. Intrinsic and engineered properties of black phosphorus. *Mater. Today Phys.* **2022**, *28*, 100895. [[CrossRef](#)]
26. Liu, X.; Ma, T.; Pinna, N.; Zhang, J. Two-dimensional nanostructured materials for gas sensing. *Adv. Funct. Mater.* **2017**, *27*, 1702168. [[CrossRef](#)]
27. Mao, S.; Chang, J.; Pu, H.; Lu, G.; He, Q.; Zhang, H.; Chen, J. Two-dimensional nanomaterial-based field-effect transistors for chemical and biological sensing. *Chem. Soc. Rev.* **2017**, *46*, 6872–6904. [[CrossRef](#)]
28. Liu, Z.; Liu, K.; Sun, R.; Ma, J. Biorefinery-assisted ultra-high hydrogen evolution via metal-free black phosphorus sensitized carbon nitride photocatalysis. *Chem. Eng. J.* **2022**, *446*, 137128. [[CrossRef](#)]
29. Zhang, L.; Wang, Z.-Q.; Liao, J.; Zhang, X.; Feng, D.; Deng, H.; Ge, C. Infrared-to-visible energy transfer photocatalysis over black phosphorus quantum dots/carbon nitride. *Chem. Eng. J.* **2022**, *431*, 133453. [[CrossRef](#)]
30. He, F.; Liu, Z.; Xu, J.; Xiong, Y.; Zhang, X.; Qi, J.; Lin, X.; Chu, C.; Shen, L.; Liu, G.; et al. Black phosphorus nanosheets suppress oxidative damage of stem cells for improved neurological recovery. *Chem. Eng. J.* **2023**, *451*, 138737. [[CrossRef](#)]
31. Chen, X.; Zhang, S.; Liu, J.; Ren, M.; Xing, D.; Qin, H. Controlling dielectric loss of biodegradable black phosphorus nanosheets by iron-ion-modification for imaging-guided microwave thermoacoustic therapy. *Biomaterials* **2022**, *287*, 121662. [[CrossRef](#)] [[PubMed](#)]
32. Donarelli, M.; Ottaviano, L.; Giancaterini, L.; Fioravanti, G.; Perrozzi, F.; Cantalini, C. Exfoliated black phosphorus gas sensing properties at room temperature. *2D Materials* **2016**, *3*, 025002. [[CrossRef](#)]
33. Lee, G.; Kim, S.; Jung, S.; Jang, S.; Kim, J. Suspended black phosphorus nanosheet gas sensors. *Sens. Actuators B* **2017**, *250*, 569–573. [[CrossRef](#)]
34. Wang, Y.; Zhou, Y.; Li, J.; Zhang, R.; Zhao, H.; Wang, Y. Ag decoration-enabled sensitization enhancement of black phosphorus nanosheets for trace NO<sub>2</sub> detection at room temperature. *J. Hazard. Mater.* **2022**, *435*, 129086. [[CrossRef](#)] [[PubMed](#)]
35. Cho, S.-Y.; Koh, H.-J.; Yoo, H.-W.; Jung, H.-T. Tunable chemical sensing performance of black phosphorus by controlled functionalization with noble metals. *Chem. Mater.* **2017**, *29*, 7197–7205. [[CrossRef](#)]
36. Liu, Y.; Wang, Y.; Ikram, M.; Lv, H.; Chang, J.; Li, Z.; Ma, L.; Rehman, A.U.; Lu, G.; Chen, J.; et al. Facile synthesis of highly dispersed Co<sub>3</sub>O<sub>4</sub> nanoparticles on expanded, thin black phosphorus for a ppb-level NO<sub>x</sub> gas sensor. *ACS Sens.* **2018**, *3*, 1576–1583. [[CrossRef](#)]
37. Wang, Y.; Zhou, Y.; Ren, H.; Wang, Y.; Zhu, X.; Guo, Y.; Li, X. Room-temperature and humidity-resistant trace nitrogen dioxide sensing of few-layer black phosphorus nanosheet by incorporating zinc oxide nanowire. *Anal. Chem.* **2020**, *92*, 11007–11017. [[CrossRef](#)]
38. Liang, T.; Dai, Z.; Liu, Y.; Zhang, X.; Zeng, H. Suppression of Sn<sup>2+</sup> and Lewis acidity in SnS<sub>2</sub>/black phosphorus heterostructure for ppb-level room temperature NO<sub>2</sub> gas sensor. *Sci. Bull.* **2021**, *66*, 2471–2478. [[CrossRef](#)]
39. Xu, Q.; Zong, B.; Yang, Y.; Li, Q.; Mao, S. Black phosphorus quantum dots modified monolayer Ti<sub>3</sub>C<sub>2</sub>T<sub>x</sub> nanosheet for field-effect transistor gas sensor. *Sens. Actuators B* **2022**, *373*, 132696. [[CrossRef](#)]
40. Cui, S.; Pu, H.; Wells, S.A.; Wen, Z.; Mao, S.; Chang, J.; Hersam, M.C.; Chen, J. Ultrahigh sensitivity and layer-dependent sensing performance of phosphorene-based gas sensors. *Nat. Commun.* **2015**, *6*, 8632. [[CrossRef](#)]
41. Lee, G.; Jung, S.; Jang, S.; Kim, J. Platinum-functionalized black phosphorus hydrogen sensors. *Appl. Phys. Lett.* **2017**, *110*, 242103. [[CrossRef](#)]
42. Chen, T.; Cheng, Z.; Tian, Q.; Wang, J.; Yu, X.; Ho, D. Nitrogen dioxide gas sensor based on liquid-phase-exfoliated black phosphorus nanosheets. *ACS Appl. Nano Mater.* **2020**, *3*, 6440–6447. [[CrossRef](#)]

43. Wang, Y.; Xue, J.; Zhang, X.; Si, J.; Liu, Y.; Ma, L.; Ullah, M.; Ikram, M.; Li, L.; Shi, K. Novel intercalated CuO/black phosphorus nanocomposites: Fabrication, characterization and NO<sub>2</sub> gas sensing at room temperature. *Mater. Sci. Semicond. Process.* **2020**, *110*, 104961. [[CrossRef](#)]
44. Liu, J.; Qu, X.; Zhang, C.; Dong, W.; Fu, C.; Wang, J.; Zhang, Q. High-yield aqueous synthesis of partial-oxidized black phosphorus as layered nanodot photocatalysts for efficient visible-light driven degradation of emerging organic contaminants. *J. Clean. Prod.* **2022**, *377*, 134228. [[CrossRef](#)]
45. Zhao, J.; Wu, S.; Liu, J.; Liu, H.; Gong, S.; Zhou, D. Tin oxide thin films prepared by aerosol-assisted chemical vapor deposition and the characteristics on gas detection. *Sens. Actuators B* **2010**, *145*, 788–793. [[CrossRef](#)]
46. Liu, J.; Liu, X.; Zhai, Z.; Jin, G.; Jiang, Q.; Zhao, Y.; Luo, C.; Quan, L. Evaluation of depletion layer width and gas-sensing properties of antimony-doped tin oxide thin film sensors. *Sens. Actuators B* **2015**, *220*, 1354–1360. [[CrossRef](#)]
47. Liu, J.; Lv, J.; Shi, J.; Wu, L.; Su, N.; Fu, C.; Zhang, Q. Size effects of tin oxide quantum dot gas sensors: From partial depletion to volume depletion. *J. Mater. Res. Technol.* **2020**, *9*, 16399–16409. [[CrossRef](#)]
48. Gu, W.; Yan, Y.; Pei, X.; Zhang, C.; Ding, C.; Xian, Y. Fluorescent black phosphorus quantum dots as label-free sensing probes for evaluation of acetylcholinesterase activity. *Sens. Actuators B* **2017**, *250*, 601–607. [[CrossRef](#)]
49. Yuan, H.; Zhao, Y.; Wang, Y.; Duan, J.; Tang, Q. Sonochemistry-assisted black/red phosphorus hybrid quantum dots for dye-sensitized solar cells. *J. Power Sources* **2019**, *410–411*, 53–58. [[CrossRef](#)]
50. Wang, Y.; Wu, X.; Liu, J.; Zhai, Z.; Yang, Z.; Xia, J.; Deng, S.; Qu, X.; Zhang, H.; Wu, D.; et al. Mo-modified band structure and enhanced photocatalytic properties of tin oxide quantum dots for visible-light driven degradation of antibiotic contaminants. *J. Environ. Chem. Eng.* **2022**, *10*, 107091. [[CrossRef](#)]
51. Liu, J.; Zhang, Q.; Tian, X.; Hong, Y.; Nie, Y.; Su, N.; Jin, G.; Zhai, Z.; Fu, C. Highly efficient photocatalytic degradation of oil pollutants by oxygen deficient SnO<sub>2</sub> quantum dots for water remediation. *Chem. Eng. J.* **2021**, *404*, 127146. [[CrossRef](#)]
52. Zhu, X.; Zhang, T.; Sun, Z.; Chen, H.; Guan, J.; Chen, X.; Ji, H.; Du, P.; Yang, S. Black phosphorus revisited: A missing metal-free elemental photocatalyst for visible light hydrogen evolution. *Adv. Mater.* **2017**, *29*, 1605776. [[CrossRef](#)]
53. Guo, Z.; Chen, S.; Wang, Z.; Yang, Z.; Liu, F.; Xu, Y.; Wang, J.; Yi, Y.; Zhang, H.; Liao, L.; et al. Metal-ion-modified black phosphorus with enhanced stability and transistor performance. *Adv. Mater.* **2017**, *29*, 1703811. [[CrossRef](#)] [[PubMed](#)]
54. Lu, B.; Zheng, X.; Li, Z. A promising photocatalyst for water-splitting reactions with a stable sandwiched P<sub>4</sub>O<sub>2</sub>/black phosphorus heterostructure and high solar-to-hydrogen efficiency. *Nanoscale* **2020**, *12*, 6617–6623. [[CrossRef](#)] [[PubMed](#)]
55. Nan, H.; Wang, X.; Jiang, J.; Ostrikov, K.; Ni, Z.; Gu, X.; Xiao, S. Effect of the surface oxide layer on the stability of black phosphorus. *Appl. Surf. Sci.* **2021**, *537*, 147850. [[CrossRef](#)]
56. Liu, J.; Lu, Y.; Cui, X.; Geng, Y.; Jin, G.; Zhai, Z. Gas-sensing properties and sensitivity promoting mechanism of Cu-added SnO<sub>2</sub> thin films deposited by ultrasonic spray pyrolysis. *Sens. Actuators B* **2017**, *248*, 862–867. [[CrossRef](#)]
57. Yamazoe, N.; Shimano, K. Theory of power laws for semiconductor gas sensors. *Sens. Actuators B* **2008**, *128*, 566–573. [[CrossRef](#)]
58. Liu, J.; Lv, J.; Xiong, H.; Wang, Y.; Jin, G.; Zhai, Z.; Fu, C.; Zhang, Q. Size effect and comprehensive mathematical model for gas-sensing mechanism of SnO<sub>2</sub> thin film gas sensors. *J. Alloys Compd.* **2022**, *898*, 162875. [[CrossRef](#)]